Three-Dimensional Numerical Simulations of Airflow Over a Heated Mountain

Terry L. Clark, National Center for Atmospheric Research[1], Boulder, Colorado 80307

Presented at the XVII OSTIV Congress, Paderborn, Germany (1981)

1. Introduction

This paper presents some numerical simulations of airflow over mountainous terrain where surface heating is important. The observations chosen for comparison are those of Raymond and Wilkening (1980) of airflow over Mt. Withington in the San Mateo range in New Mexico on 5 June 1978. In the case chosen the response is mainly forced by the elevated heating of the mountain. The main purpose of this work is to assess our ability to predict heated terrain response by comparing model data with aircraft observations.

Earlier simulations of airflow over small-scale topography using numerical models have been presented by Gal-Chen and Sommerville (1975a, b), Orville (1965), Clark and Peltier (1977), Klemp and Lilly (1978), and Peltier and Clark (1979), among others. The first three of these studies concentrated on two-dimensional simulations of elevated heating cases and the last three on more purely dynamical responses in the study of downslope windstorms. The last two papers were quite successful in their attempts to better understand downslope windstorms by comparing model and observational data.

2. Model description

a. Basic model

The numerical model employed is the model of Clark (1977). The model is a three-dimensional, non-hydrostatic finite-difference model using second order time and space differencing schemes. In order to accommodate irregular surface terrain features a coordinate transformation has been employed where variables in Cartesian (x, y, z) have been transformed to $(x, y, \bar{z})$ where

$$\bar{z} = (z-h)H/(H-h),$$

and h = h(x,y) is the height of the terrain above some base level and H is the height of the fixed model «lid.»

b. Surface heating rate

The treatment of surface heating was considered in two levels of complexity. Experiment MW-2 allowed for a time varying estimate of the surface heating rate, S, depending on the sun's zenith angle;

$$S = S_0 \cos Z, \quad (1)$$

where S_0 is the solar constant taken as 1395 watts/m^2, Z the sun's zenith angle, and μ a factor to account for absorption and reflection. μ = .50 was used for both Exps. MW-2 and MW-3.

Applying (1) to a model simulation, with surface topography, treats elevated heating effects but does not consider the difference in heating rates between surfaces facing into and away from the sun. Following Sellers (1965), the effects of sloping terrain were incorporated for Exp. MW-3.

3. Model results

Figure 1 shows the profiles used to initialize the Mt. Withington experiments. An aircraft sounding was used to define the upstream flow conditions. The initial conditions below 2 km AGR (above ground reference of 2000 m MSL) had strong directional shear but no speed shear. In this case the wind backs from the north near the surface to the west at 2 km AGR. Above 2 km the wind direction is from the west and the wind speed increases almost linearly with height, reaching a maximum at 6 km AGR of about 11 m s^{-1}. The atmosphere was stably stratified initially except for a neutral layer near 2.5 km.

The development of the airflow over Mt. Withington can be described by the following sequence of physical regimes. First, the predawn dynamic response is due entirely to flow over and around the topography, since predawn conditions assume zero surface sensible heat flux. Second, an early morning heating response which appears mainly as an intensification of the predawn flow and third, around mid-morning, a regime of well-defined longitudinal rolls appears. This progression of regimes occurred for both experiments.

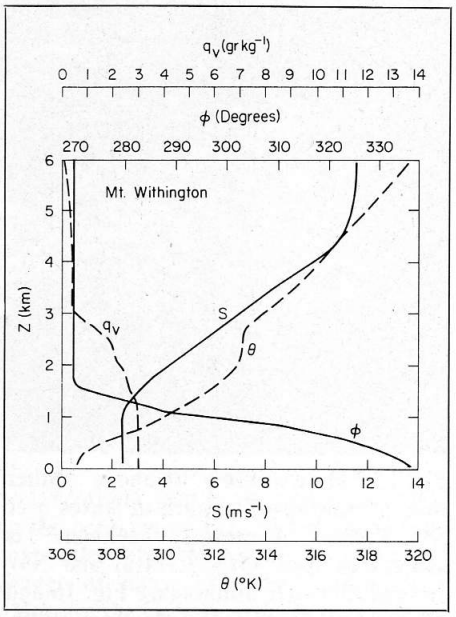

Figure 1 The environmental conditions used in the Mt. Withington numerical simulations are shown. Shown in the figure are the wind speed, s, and direction, Φ, the potential temperature, Θ, and the water vapor mixing ratio, q_v.

Figure 2 shows cross-sectional plots from the two experiments of the vertical velocity, w, at three times. The first plot is from Exp. MW-2 just prior to sunrise (5:00 a. m.). It shows rather dynamic fields but with evidence of lee waves filling the lower troposphere. The maximum magnitude of w within these waves is approximately .12 m s^{-1}. At 8:00 a. m. in the plot from Exp. MW-3 there is a considerable intensification of the earlier pattern with a maximum in excess of 1 m s^{-1}. By 8:40 a. m. continued heating has produced an abrupt onset of longitudinal rolls within the boundary layer and the further intensification of the lee waves.

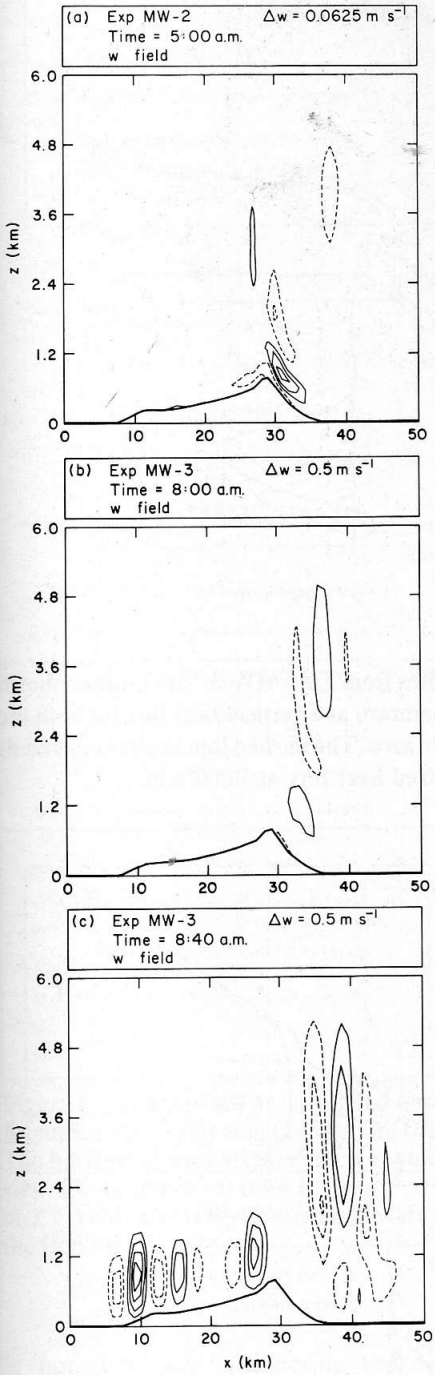

Figure 2 Cross-section plots of vertical velocity, w, from Exps. MW-2 and MW-3. The three plots are all for y = 25 km. Heavy solid lines represent the ground surface. Solid contours represent positive values whereas dashed represent negative values. The heavy contour outlines the mountain for this cross-section. The three-dimensional shape of the mountain is basically elliptical with the mountain extending about 25 km in the north-south direction.

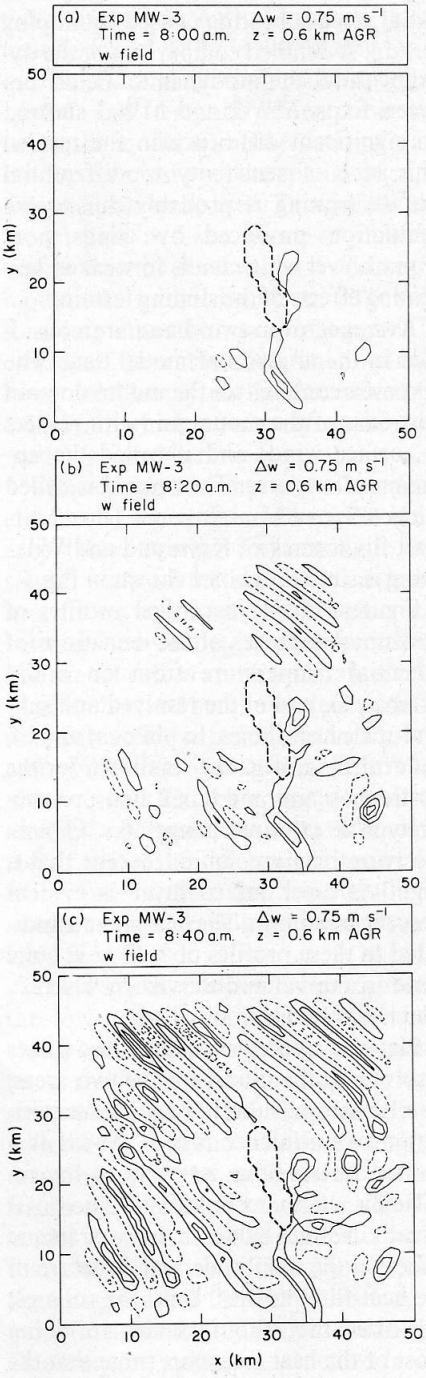

Figure 3 Plan views of w for z = .6 km above the ground reference level of 2000 m MSL. The heavy dashed contours represent a rough outline of the mountain at this height. Contour intervals and times are shown on figures.

The development of w in the boundary layer from the early to mid-morning regimes is shown in Fig. 3 for Exp. MW-3. These figures depict horizontal plan view plots of w at the constant altitude of .6 km AGR for 8:00, 8:20 and 8:40 a. m. A ridge of the mountain protrudes above this altitude. At 8:00 a. m. in Fig. 3(a) there are no clear signs of longitudinal rolls although a reduced contour interval would show them developing in portions of the model domain. By 8:20 a. m. the rolls are now apparent over a large area and by 8:40 are as well organized as they will get for the present simulation. These rolls parallel the average of the wind shear vector over their depth.

One point of interest in the present pair of simulations is the effect of differential surface heating caused by sloping terrain. A detailed comparison of the dynamic and thermodynamic fields between Exps. MW-2 and MW-3 showed no significant difference in the results. This lack of sensitivity to differential surface heating is probably due to the ventilation produced by winds near ground level which tends to weaken any heating effects of the sloping terrain.

Averages over two areas are considered in the analysis of model data. The first area contains all the model domain upstream of the mountain (with respect to surface wind) and is called the upstream plains area. The second is called the box 2 (or mountain) area. (Box 2 aircraft flight track of Raymond and Wilkening is similar to box 1 shown in Fig. 6.)

Figure 4 displays vertical profiles of horizontal averages of the deviations of potential temperature from an initial adiabat, Θ, and of the resolved and subgrid-scale heat fluxes. In plates a) and b), the evolution of $< \Theta >$ is shown for the upstream plains and box 2 areas, respectively. The rates of change of $< \Theta >$ in the two areas are similar except that a slightly deeper mixed layer is evident over the mountain. The heating rate indicated in these profiles of $< \Theta >$ is quite close to the value observed by aircraft, which was 1.50 K h^{-1}.

Plates c) and d) show the heat fluxes resolved by the model for the two areas. The 10:00 a. m. subgrid scale parameterization of turbulence is also shown as a dashed line. Above z ~ 400 m the resolved-scale fluxes dominate. The onset of rolls at about 8:00 a. m. has a dramatic effect on the amplitude and structure of the heat flux profiles. Until the rolls get organized the sub-grid scales are doing most of the heat transport (note that the resolved-scale heat flux over the upstream plains area is nearly zero at 8:00 a. m.). After the development of the rolls the resolved-scale fluxes are dominant through much of the upper part of the boundary layer. The onset of organized convection is earlier over the mountain as can be seen by the differences between the 8:00 a. m. profiles of heat flux. Furthermore, the intensity of the heat flux is higher over the mountainous area which

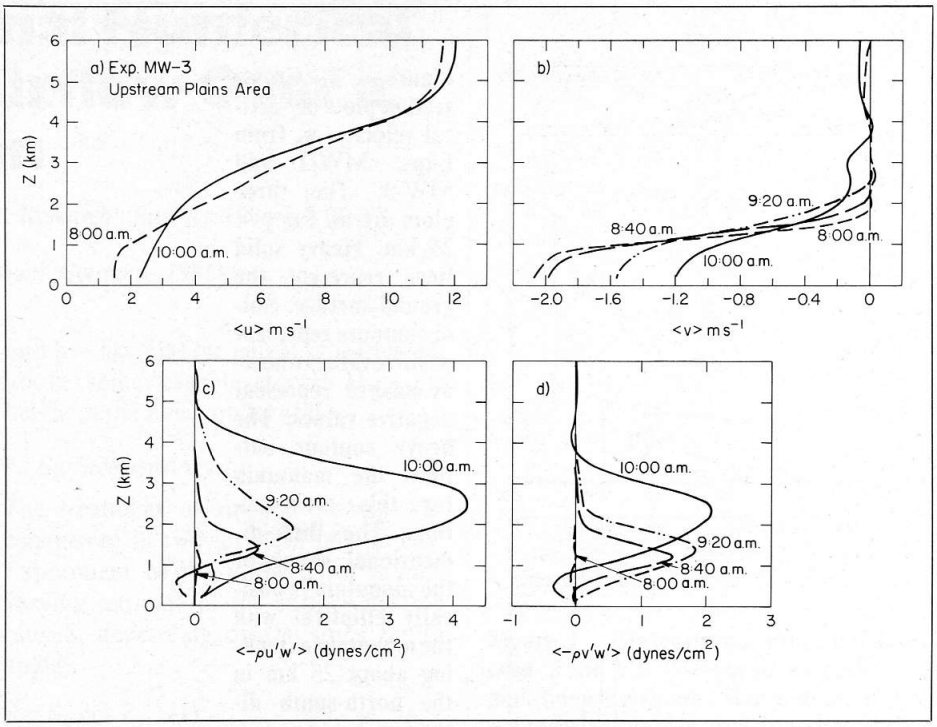

Figure 4 Time sequence plots of vertical profiles from Exp. MW-3. The profiles shown are area-averaged perturbation potential temperature and vertical heat flux for both the upstream plains area and for the box 2 mountain area. The dashed line in plates c) and d) represents the mean subgrid scale parameterized heat flux at 10:00 a.m.

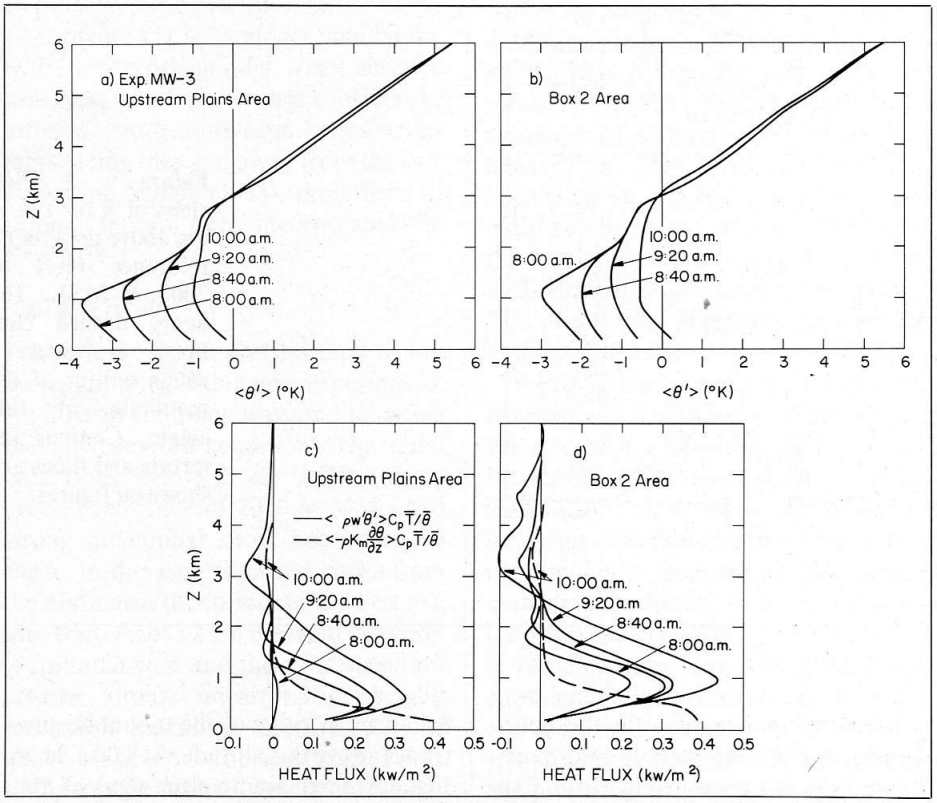

Figure 5 Time sequence plots of vertical profiles from Exp. MW-3. The profiles shown are areal average values of easterly wind speed, u, and northerly wind speed, v, and the corresponding Reynolds stress terms. The area chosen is the upstream plains area.

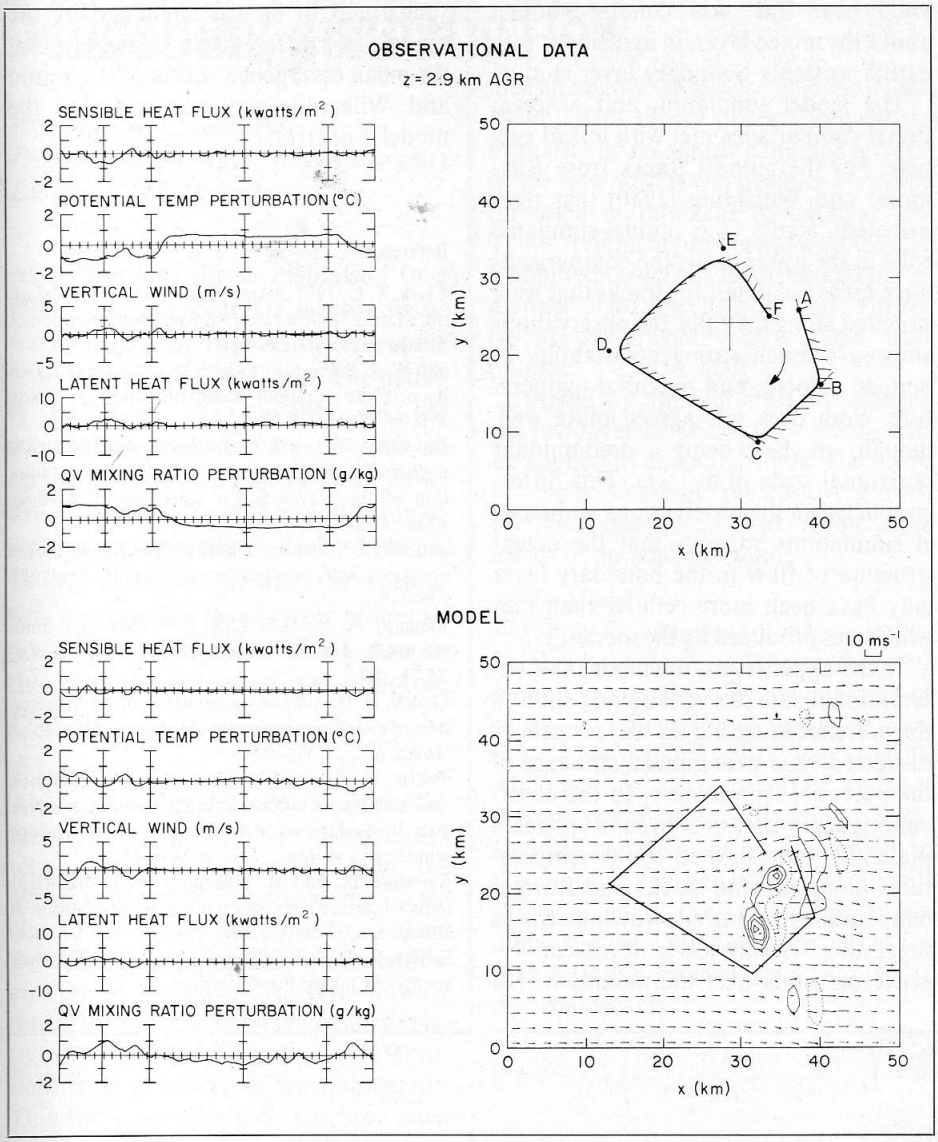

Figure 6 Comparison of model and observational data for the aircraft box reported in Raymond and Wilkening (1980). The flight track is shown in the right-hand plan views. The horizontal wind vectors and w contours (for model only) are also shown in the plan view. Contour interval for w is 1 m s^{-1}. This figure is for box 1 flight which is at a height of 2.9 AGR. The vertical bars on the left side of the figure correspond to points A to F of the flight track.

is not surprising considering the enhanced forcing due to the elevated heating source.

Figure 5 displays the evolution of the horizontal velocity components and the related vertical stress terms. The stress patterns in general exhibit flux convergence in the upper levels. Overall, plates a) through d) suggest a positive transfer of energy from the mean flow to the eddies which is the expected result. One aspect that is quite apparent is the explosive increase in the magnitude and vertical extent of the Reynolds stress, $<-\varrho v'w'>$, between 9:20 a. m. to 10:00 a. m. The timing of this event coincides with the penetration of boundary layer convection into the neutral layer that existed in the initial sounding. It is likely that it was this event that produced the large growth rates in the Reynolds stress profiles.

Figure 6 displays a comparison between the observational and model data, for five variables, for the box 1 flight track level: the sensible heat flux, potential temperature, vertical velocity, latent heat flux, and water vapor mixing ratio, q_v. There are some slight differences in spatial and temporal orientation between the model and observational data but for the most part the spatial orientation matches quite well. Temporally the model data is taken about 40 minutes earlier than the observations because the model was initiated with an 8:00 a. m. sounding instead of, say, 5:00 a. m. The erosion of the stable nocturnal boundary layer was already partially achieved by 8:00 a. m. which effectively pushes the model forward in time.

Considering the simplicity of the model some of the comparisons seem quite acceptable. Overall, the amplitude and spatial scale of the sensible and latent heat fluxes are in reasonable agreement between the model and observations. The model values are slightly larger than what is observed but the tendency for the strongest action to be just east and southeast of the ridge is in agreement with the observations. However, too serious an attempt at point-by-point comparison of any of these fields is not warranted because of the strong local gradients along the flight track in the model-simulated fields.

The vertical velocity comparisons at the lower levels (not shown) are best along tracks that cross the model-simulated rolls where both amplitude and structure of the w fields show agreement with the observations. The poorest agreement between the w fields occurs on tracks parallel to the model rolls. The model shows a much larger spatial scale than the observations. Thus, the observations suggest that the true fields may be more finely structured than in the model. One may interpret the structure in the observations as being more cellular. In box 1 of Fig. 6 at z = 2.9 km, where the flow downstream of the mountain contains lee waves rather than the rolls, there is some support in the observations for the existence of lee waves. The pattern of w along the flight tracks from A to C shows very strong similarities between the observations and model simulations.

With Θ', as with the w field, the stron-

gest comparison is at the lower levels on the northern track across the rolls and the poorest comparison along the western tracks parallel to the rolls. One rather noticeable difference between the model and observations in the Θ' field is in box 1 of Fig. 6 where the observations show a rather large-scale trend with Θ' positive over 40 km of the track and negative over the remaining 28 km. This trend is not at all apparent in the model field. The warm Θ downstream and the cool Θ upstream suggest an overall low-level convergence of the flow over the mountain which did not develop in the simulations.

The horizontal velocities are also shown in Fig. 6 for both the model and observations. The high level data of box 1 in Fig. 6 compare favorably whereas significant differences are apparent in the lower levels.

5. Conclusions

Analysis of the momentum and heat flux profiles showed that the fluxes were dominated by the resolved scales of the model for elevations approximately 400 m or more above the surface. The momentum fluxes tended to alter the mean flow from a strongly backing wind towards a veering profile. The resolved scale heat flux was counter-gradient above the mixed layer, in agreement with earlier unstable boundary layer studies.

The model simulation and observational comparisons met with mixed success. For the aircraft tracks from Raymond and Wilkening (1980) that were oriented across the model-simulated rolls in the lower levels the comparisons were quite good; but for tracks that were oriented along the rolls, the observations showed a much stronger variability of vertical velocity and potential temperature. Both data sets agreed quite well, though, on there being a predominant horizontal scale of 5–7 km. This difference between the observations and model simulations suggests that the actual structure of flow in the boundary layer may have been more cellular than that which was produced by the model.

In the upper levels, the model and observational data sets consistently showed the presence of strong lee waves but they disagreed on a pronounced structure of the potential temperature. In the observations at $z = 2.9$ km above the upstream plains the data showed cooler temperatures along upwind tracks and warmer temperatures along downwind tracks suggesting overall lower level convergence of winds over the mountain. No such trend in Θ was simulated by the model. This difference in Θ suggests that the mean divergence values of Raymond and Wilkening are real and that the model is in error.

References

Clark, T. L., 1977: A small scale dynamic model using a terrain-following coordinate transformation. *J. Comput. Phys., 24,* 186–215.

and **W. R. Peltier,** 1977: On the evolution and stability of finite-amplitude mountain waves. *J. Atmos. Sci., 34,* 1715–1730.

Gal-Chen, T., and **R. C. J. Sommerville,** 1975a: On the use of a coordinate transformation for the solution of the Navier-Stokes equations. *J. Comput. Phys., 17,* 209–228.

and 1975b: Numerical solution of the Navier-Stokes equations with topography. *J. Comput. Phys., 17,* 276–310.

Klemp, J. B., and **D. K. Lilly,** 1978: Numerical simulation of hydrostatic mountain waves. *J. Atmos. Sci., 35,* 78–107.

Orville, H. D., 1965: A numerical study of the initiation of cumulus clouds over mountainous terrain. *J. Atmos. Sci., 22,* 684–699.

Peltier, W. R., and **T. L. Clark,** 1979: The evolution and stability of finite-amplitude mountain waves. Part II: Surface wave drag and severe downslope windstorms. *J. Atmos. Sci., 36,* 1498–1529.

Raymond, D., and **M. Wilkening,** 1980: Mountain-induced convection under fair weather conditions. *J. Atmos. Sci., 37,* 2693–2706.

Sellers, W. D., 1965: *Physical Climatology.* The University of Chicago Press, Chicago.